Monthly Notices of the ROYAL ASTRONOMICAL SOCIETY

MNRAS **485,** 1595–1613 (2019)
Advance Access publication 2019 January 18

doi:10.1093/mnras/stz202

Multiphase circumgalactic medium probed with MUSE and ALMA

Céline Péroux,[1★] Martin A. Zwaan,[2] Anne Klitsch,[2,3] Ramona Augustin,[1,2] Aleksandra Hamanowicz,[2] Hadi Rahmani,[1,4] Max Pettini,[5] Varsha Kulkarni,[6] Lorrie A. Straka,[7] Andy D. Biggs,[2] Donald G. York[8] and Bruno Milliard[1]

[1]*Aix Marseille Université, CNRS, LAM (Laboratoire d'Astrophysique de Marseille) UMR 7326, F-13388 Marseille, France*
[2]*European Southern Observatory (ESO), Karl-Schwarzschild-Str.2, D-85748 Garching b. München, Germany*
[3]*Department of Physics, Centre for Extragalactic Astronomy, Durham University, South Road, Durham DH1 3LE, UK*
[4]*GEPI, Observatoire de Paris, PSL Université, CNRS, 5 Place Jules Janssen, F-92190 Meudon, France*
[5]*Institute of Astronomy, University of Cambridge, Madingley Road, Cambridge CB3 0HA, UK*
[6]*Department of Physics and Astronomy, University of South Carolina, Columbia, SC 29208, USA*
[7]*Sterrewacht Leiden, Leiden University, PO Box 9513, NL-2300 RA Leiden, the Netherlands*
[8]*Department of Astronomy and Astrophysics, The Enrico Fermi Institute, University of Chicago, 5640 S. Ellis Ave, Chicago, IL 60637, USA*

Accepted 2019 January 15. Received 2019 January 15; in original form 2018 August 1

ABSTRACT

Galaxy haloes appear to be missing a large fraction of their baryons, most probably hiding in the circumgalactic medium (CGM), a diffuse component within the dark matter halo that extends far from the inner regions of the galaxies. A powerful tool to study the CGM gas is offered by absorption lines in the spectra of background quasars. Here, we present optical (MUSE) and mm (ALMA) observations of the field of the quasar Q1130−1449 which includes a log $[N(\mathrm{H\,I})/\mathrm{cm}^{-2}] = 21.71 \pm 0.07$ absorber at $z = 0.313$. Ground-based VLT/MUSE 3D spectroscopy shows 11 galaxies at the redshift of the absorber down to a limiting SFR > 0.01 $\mathrm{M}_\odot\ \mathrm{yr}^{-1}$ (covering emission lines of [O II], Hβ, [O III], [N II], and Hα), 7 of which are new discoveries. In particular, we report a new emitter with a smaller impact parameter to the quasar line of sight ($b = 10.6$ kpc) than the galaxies detected so far. Three of the objects are also detected in CO(1–0) in our ALMA observations indicating long depletion time-scales for the molecular gas and kinematics consistent with the ionized gas. We infer from dedicated numerical cosmological RAMSES zoom-in simulations that the physical properties of these objects qualitatively resemble a small group environment, possibly part of a filamentary structure. Based on metallicity and velocity arguments, we conclude that the neutral gas traced in absorption is only partly related to these emitting galaxies while a larger fraction is likely the signature of gas with surface brightness almost four orders of magnitude fainter that current detection limits. Together, these findings challenge a picture where strong-N(H I) quasar absorbers are associated with a single bright galaxy and favour a scenario where the H I gas probed in absorption is related to far more complex galaxy structures.

Key words: galaxies: abundances – intergalactic medium – galaxies: ISM – galaxies: kinematics and dynamics – quasars: absorption lines.

1 INTRODUCTION

Baryons are missing from galaxies in what is known as the galaxy halo missing baryon problem (McGaugh 2008). Indeed, galaxy haloes appear to be missing approximately 60 per cent of their baryons compared to expectations from the cosmological mass density, suggesting that these are structures nearly devoid of baryons both in mass and spatial extent. It has become apparent that galaxies also exhibit a diffuse baryonic component within the dark matter halo that extends far from the inner regions to the virial radius and beyond. This halo gas or circumgalactic medium (CGM) has been partly detected in the hot gas emitted around galaxies and detected in the X-rays regime (e.g. Anderson & Bregman 2010; Bregman et al. 2018; Nicastro et al. 2018) as well as in Ly α (e.g. Wisotzki et al. 2016; Leclercq et al. 2017; Wisotzki et al. 2018). On the other hand, a powerful tool to study the cooler gas is offered by absorption lines in the spectra of background quasars as it allows us to study

★ E-mail: celine.peroux@gmail.com

underdense gas regions with a sensitivity independent of redshift (e.g. Morris et al. 1993; Tripp, Lu & Savage 1998). Observations of redshifted UV absorption lines have indeed revealed much lower temperature and density gas in the CGM (Steidel et al. 2010; Rudie et al. 2012; Werk et al. 2013; Turner et al. 2014).

A remaining challenge is to relate the gas traced in absorption to the galaxy properties. A particularly powerful technique to bridge the gas component and stellar content of galaxies has come from integral field spectroscopy (IFS). Over the past few years, this technique has been used to study the CGM of high-redshift galaxies using near-infrared Integral Field Units (IFUs) by successfully detecting the galaxies responsible for strong-H I absorbers at redshifts $z \sim 1$ and $z \sim 2$ in H α and [N II] emission (Bouché et al. 2007; Péroux et al. 2011a,b; Rudie, Newman & Murphy 2017). Together with long slit spectroscopy follow-up, these observations have enabled us to map the kinematics, star formation rate (SFR), and metallicity of this emission-line gas, and to estimate the dynamical masses of these galaxies (Bouché et al. 2012; Péroux et al. 2012; Bouché et al. 2013; Péroux, Kulkarni & York 2014). As optical IFUs became available, the study of the CGM using absorption techniques has expanded (Schroetter et al. 2015; Bielby et al. 2017; Bouché et al. 2016; Fumagalli et al. 2016; Bielby et al. 2018) to also include lower redshift objects (Péroux et al. 2017; Klitsch et al. 2018; Péroux et al. 2018; Rahmani et al. 2018a).

Here, we present results from new MUSE and ALMA observations of the field of background quasar Q1130−1449 with a strong-H I absorber at $z_{\rm abs} = 0.313$. The manuscript is organized as follows: Section 2 presents the observational set-up and data reduction. Section 3 details the analysis and results derived from these data, while Section 4 summarizes our findings. Throughout this paper we adopt an $H_0 = 70\,{\rm km\,s^{-1}\,Mpc^{-1}}$, $\Omega_{\rm M} = 0.3$, and $\Omega_\Lambda = 0.7$ cosmology. At the redshift of the absorber, 1 arcsec corresponds to 4.6 kpc.

2 OBSERVATIONS OF THE Q1130−1449 FIELD

2.1 Quasar spectroscopy: absorption properties

The $z_{\rm QSO} = 1.189$ ($V = 16.9$ mag) quasar (J2000 coordinates: 113007.05−144927.38; alternative name: PKS B1127−145) sight-line intersects three Mg II absorption systems: $z_{\rm abs} = 0.191$ (Kacprzak, Murphy & Churchill 2010), 0.313 (Bergeron & Boisse 1991), and 0.328 (Narayanan et al. 2007). We here concentrate on the middle redshift absorber, while Hamanowicz et al. (in preparation) presents the other two systems.

From a *HST*/Faint Object Spectrograph (FOS) UV spectrum, the $z_{\rm abs} = 0.313$ absorber was determined to be a damped Ly α (DLA) system with a large H I column density of neutral gas: log [N(H I)/cm^{-2}] = 21.71 ± 0.07 (Lane et al. 1998). Lane et al. (1998) also detected 21cm absorption spanning FWHM = 42.1 ± 2.7 km s^{-1} at the redshift of that absorber with the Westerbork Synthesis Radio Telescope (WSRT). This was later confirmed by Kanekar et al. (2009) who derived a spin temperature $T_{\rm spin} = 820 \pm 145$K and covering factor, $f = 0.9$ from Very long baseline interferometry (VLBI) observations. Bechtold et al. (2001) additionally reported strong X-ray absorption in excess of the Galactic value in the Chandra quasar spectrum which they interpreted as associated with that absorber. Based on this assumption, they derived the abundance of the oxygen group elements, independently of dust depletion, of 23 per cent solar. Kanekar et al. (2014) computed the zinc metallicity to be [Zn/H] = −0.80 ± 0.16 relative to solar (i.e. the neutral gas metallicity is 16 per cent solar) from a medium-resolution *HST*/STIS spectrum. Guber, Richter & Wendt (2018) used the VLT/UVES spectrum of the quasar to fit the multicomponent profile in Ti, Mn, and Ca which are likely depleted into dust grains. In addition, they estimated the H I column density of each component from the observed Ca II column density pattern, assuming a constant Ca II/H I ratio. Interestingly, the thus estimated H I column density for each component, on its own, exceeds the canonical DLA definition (log [N(H I)/cm^{-2}] > 20.3).

We obtained the VLT/UVES reduced quasar spectra from the ESO advanced data products archives.[1] Fig. A1 of the Appendix A presents our independent fit to the metal absorption profiles, which is consistent with findings from Guber et al. (2018), adding lines from Fe II, Mg I, and the saturated Mg II doublet. The zero velocity in the figure is set to the systemic redshift of galaxy G0, $z_{\rm G0} = 0.31305$ (see later section). Most of the absorption lies blueward of this systemic redshift.

2.2 Field Imaging: identifying absorbing galaxies

2.2.1 New MUSE observations

We report new MUSE medium-deep (5-h on source) observations of this field. The observations were carried out in service mode (under programme ESO 96.A-0303, PI: C. Peroux) during the nights of 2015 December 7–8 ($T_{\rm exp} = 4 \times 960$ s), 2016 March 5–6 (4 × 1200 s) and 2017 February 19–20 (8 × 1200 s). The seeing constraint for these observations was < 0.8 arcsec and natural seeing mode was used. The field was rotated by 90 deg between exposures. These were further divided into two equal sub-exposures, with an additional field rotation of 90 deg and sub-arcsec dithering offset in two-step pattern to minimize residuals from the slice pattern. The field of view is 60 × 60 arcsec, corresponding to a 0.2 arcsec/pixel scale. We used the 'nominal mode' resulting in a spectral coverage of ∼4800–9300 Å. At the redshift of the target ($z_{\rm abs} = 0.313$), the data cover emission lines from [O II]$\lambda\lambda$3727, 3729 to H α. The spectral resolution is R= 1770 at 4800 Å and R = 3590 at 9300 Å resampling the whole spectrum to a spectral sampling of 1.25 Å/pixel.

The ESO MUSE pipeline (Weilbacher 2015) version v1.6 was used to reduce the data together with additional external routines for sky subtraction and extraction of the 1D spectra. We used master bias, flat-field images, and arc lamp exposures from observations taken closest in time to the science frames to correct each raw cube. We processed the raw science data with the *scibasic* and *scipost* recipes, correcting the wavelength calibration to a heliocentric reference. The wavelength solutions were checked using the known wavelengths of the night-sky OH lines and were found to be accurate within 15 km s^{-1}. We centred the individual exposures with the *exp_align* recipe using the point sources in the field to ensure accurate relative astrometry. We combined the individual exposures into a single data cube using the *exp_combine* recipe. We measured the seeing of the final combined data from the quasar and other bright point sources in the cube. We calculated that the point spread function (PSF) has a full width at half-maximum (FWHM) of 0.76 arcsec. Finally, to estimate the flux uncertainty, we compared the flux calibration with the R magnitude of the quasar and a bright star in the field. We computed the MUSE broad-band fluxes in the R-band filter. We determined the flux error to be ±25 per cent.

[1] http://archive.eso.org/cms.html

The removal of OH emission lines from the night sky was accomplished with an additional purpose-developed code. The *scipost* recipe was performed with sky-removal method turned off. After selecting sky regions in the field, we created PCA components from the spectra which were further applied to the science data cube to remove sky line residuals (Husemann et al. 2016; Péroux et al. 2017). The resulting MUSE white light image is shown on the right-hand panel of Fig. 1. We retrieved *HST*/WFPC2 F814W image of the field from the *HST* archive, and we show it on the left-hand panel of Fig. 1.

2.2.2 *New ALMA observations*

The field of Q1130−1449 was observed with ALMA in Band 3 to cover the CO(1–0) emission lines at the redshift of the $z_{\rm abs} = 0.313$ absorber (under programme 2016.1.01250.S, PI: C. Peroux) on 2016 December 4, 8, and 15. The precipitable water vapour (PWV) varied between 1.5 and 5.4 mm and the total on-source observing time was $T_{\rm exp} = 3.6$ h. A compact antenna configuration (C40-3) resulted in an angular resolution 1.2 × 1.8 arcsec. One of the four spectral windows was centred on the redshifted CO(1–0) line frequency of 87.8 GHz and used the high spectral resolution mode, providing 3840 channels of each 0.488 MHz wide. The other three spectral windows were set to low spectral resolution mode and were used for continuum observations of the field. The quasars J1058+0133 and J1139−1350 were used as amplitude and phase calibrators, respectively.

We started the data reduction with the pipeline-calibrated uv-data sets, as delivered by ALMA. Additional data reduction steps were carried out with the COMMON ASTRONOMY SOFTWARE APPLICATIONS (CASA) software package version 4.7.0. Minor manual flags were added to remove some uv-data points with strongly outlying amplitudes. Next, we applied two cycles of self-calibration on the data. The quasar in the centre of our science field is very bright at mm frequencies (∼800 mJy), which makes the field very suitable for self-calibration of both the phases and amplitudes.

First, we used the *tclean* recipe to Fourier transform the uv-data into a continuum image. The self-calibration procedure was performed using the tasks *gaincal* and *applycal* on individual measurement sets to create corrected uv-data, after which the data were re-imaged to create an improved continuum map. We applied one round of phase self-calibration and one round of amplitude and phase self-calibration. The next step was to subtract the bright continuum source from the field using the task *uvsub*. We then built a cube with the *tclean* task, setting the pixel size to 0.2 arcsec, so as to oversample the beam sufficiently, and using a 'robust' weighting scheme with a Briggs parameter of 0.5. One of the four spectral windows was centred on the redshifted CO(1–0) line frequency of 87.8 GHz and used the high spectral resolution mode, using a binning of 8, providing 3840 channels of each 3.906 MHz wide. We applied a spectral binning of seven channels to achieve a velocity resolution of 53 km s^{-1}. We removed remaining continuum signatures around the imperfectly subtracted quasar with the *uvcontsub* task. Lastly, we produced a cube corrected for the primary beam using the *pbcor* task. The final rms noise level of the cube is 0.11 mJy beam^{-1} per 53 km s^{-1} channel, and the angular resolution is 1.4 × 1.3 arcsec, corresponding to 6 kpc at the redshift of the target. We note that the resulting FWHM of the primary beam of ALMA in band three is about 60 arcsec, conveniently matching the MUSE field of view

In addition, we created a small cube around the quasar with the highest spectral resolution (∼7 km s^{-1}) to search for absorption lines, but do not detect the CO(1–0) absorption line at the absorber redshift in the spectrum of the background quasar. Given the rms, we compute an optical depth limit of $\tau = 0.0125$ km s^{-1} at 5σ assuming a 10 km s^{-1} wide absorption line following Zwaan et al. (2015) calculation. Assuming the excitation temperature equates the $T_{\rm CMB}$ at $z = 0.313$, we derive a stringent limit on the CO column density of N(CO)<2 × 10^{13} cm^{-2} (Mangum & Shirley 2015). Using the mean CO/H_2 column density ratio of 3 × 10^{-6} from Burgh, France & McCandliss (2007), this results in a limit of N(H_2) < 7 × 10^{18} cm^{-2}.

3 ANALYSIS AND RESULTS

3.1 The environment of $z_{\rm abs} \sim 0.3$ H I-rich absorbers

3.1.1 *Galaxies at $z_{abs} = 0.313$ in the field of Q1130−1449*

The field is part of an observing campaign targeting quasar absorbers whose redshifts allow detection of H α with MUSE, with measured N(H I) from *HST* UV spectroscopy and a known associated galaxy. On top of this, the field of Q1130−1449 has been the target of a number of observing programs in the past which we summarize here. We use the numbering system introduced by Kacprzak et al. (2010) when relevant and add to it for the new detections. Fig. 1 illustrates this naming scheme. Bergeron & Boisse (1991) first reported emission (and absorption) lines at the redshift of the absorber in two objects (G2 and G4). Deharveng, Buat & Bergeron (1995) had successfully detected H β (but no Ly α) in G2 from *HST*/FOS spectroscopy. Lane et al. (1998) later obtained a spectroscopic redshift of another galaxy (G1) which is also consistent with the absorption redshift. Kacprzak et al. (2010) spectroscopically identified two additional galaxies (G6 and G14), the latter of which is outside our MUSE field.

Here, we used the *HST* images as a prior to extract spectra from the MUSE cube. To this end, we used SEXTRACTOR to identify and deblend faint objects in the broad-band WFPC2 image. Using the MPDAF[2] routine (Piqueras et al. 2017), we extract the pixels at these coordinates above a 0.75σ threshold. We then reviewed the extracted spectra to identify those matching $z_{\rm abs} = 0.313$. In some cases, no emission lines were detected, but strong Ca II absorption lines and a Balmer break matching $z_{\rm abs} = 0.313$ were identified (e.g. G20). In addition, we made pseudo-narrow-band images of the MUSE cube at the expected position of the emission lines. An example of this is shown in Fig. 2 (top panel) for [O III] 5007 Å and Fig. 4 (top panel) for H α. This approach reveals additional objects which remain undetected in the *HST* image because of their faint continuum level (e.g. G0, G16, and G17).

In particular, we discovered a faint object, G0, closer to the quasar at impact parameter $b = 2.3$ arcsec (10.6 kpc). We note that it is not matched by any object detected in Gemini AO-images by Chun et al. (2006) because of the different wavelength coverage (optical versus H band) and different sensitivity (emitters versus continuum objects). While the object lies under the quasar PSF, several emission lines are clearly identified in the MUSE spectrum. In the following analysis, we use the systemic redshift of G0 as reference for the analysis of the absorption profile plotted in velocity (see Appendix A) simply because it has the smallest impact parameter

[2] http://mpdaf.readthedocs.io/en/latest/index.html

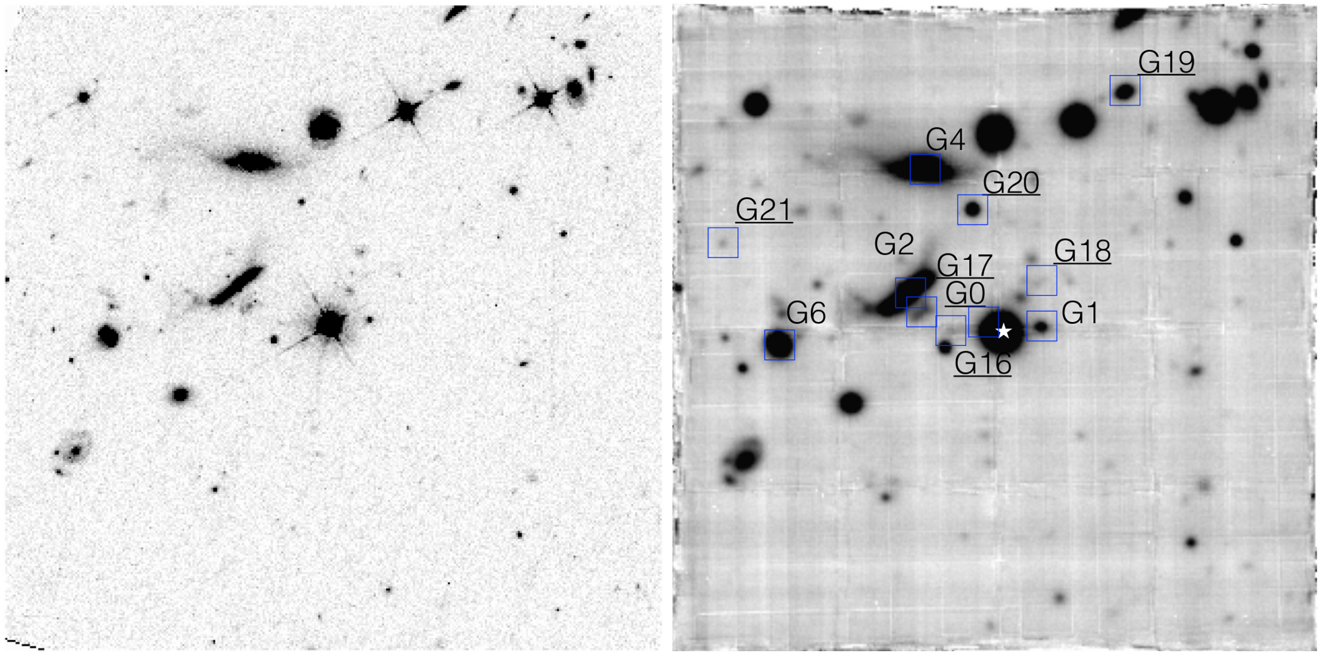

Figure 1. *HST* /WFPC2 F814W image of the quasar field (left-hand panel) and MUSE white light image (right-hand panel) showing objects with bright continua. The exposure time for the *HST* image is 4400 s, while for MUSE it is 14 400 s. The quasar is at the centre of the image. North is up, East to the left. The fields of view are $\sim 1 \times 1$ arcmin. MUSE observations additionally provide spectroscopic and kinematic information for the majority of the objects in the field. The quasar is shown as a white star and the positions of the galaxies associated with the quasar absorber are marked with light blue squares. Four of the galaxies previously identified are detected (namely G1, G2, G4, and G6) and their numbering system follows Kacprzak et al. (2010). The other seven objects (G0 and >G16, underlined) are new identifications at $z_{\rm abs} = 0.313$. Some objects are bright in the continuum but undetected in pseudo-narrow-band images because of weak emission lines (i.e. G4, G20, and G21).

to the quasar of all objects spectroscopically detected in the field. In essence, this system is like the 'Galaxies with background QSOs' searches which have found quasars shining through low redshift, foreground galaxies at small impact parameters (<10 kpc) within the SDSS fibres (York et al. 2012; Straka et al. 2013; Straka et al. 2015; Joshi et al. 2017). These, together with recent findings of low impact parameter objects in high spatial resolution *HST* imaging (i.e. Augustin et al. 2018), provide observational evidence to the postulate of York et al. (1986) that 'some quasar absorption-line systems may arise when a quasar sightline intersects a Magellanic-type irregular galaxy (i.e. a gas-rich dwarf)'. Fig. 1 (right-hand panel) summarizes the numbering system of the new identifications. The corresponding MUSE spectra are displayed in Fig. 5. In total, we report 11 objects at the redshift of the absorber in our MUSE data, 7 of which are new discoveries.

Similarly, we identified the galaxies at the absorber redshift in the ALMA observations by running the DUCHAMP[3] source finder (version v1.6.2) which performs a three-dimensional search via wavelet reconstruction with a detection threshold of 5σ on the cube before primary beam correction. We find three secure emitters associated with galaxies G2, G4, and G6, respectively. Fig. 3 shows the CO(1–0) contours overlaid on the background *HST* image. In addition, we performed a visual inspection of the cube at the redshifted frequency of the CO(1–0) line. We detect a fourth emission line, 26.4 arcsec south of the quasar. The MUSE spectrum shows a featureless continuum object consistent with either CO(2–1) at $z = 1.614$ or CO(3–2) at $z = 2.921$ (a higher CO transition would have matching Lyα line in the MUSE spectrum).

Interestingly, one of the continuum spectral window also reveals an emission line at 101.4 GHz which is identified as CO(2–1) at $z = 1.274$ thanks to the detection of the [O II] doublet in the corresponding MUSE spectrum. These findings illustrate the power of combining ALMA with MUSE observations to securely assess the redshift of single line mm detections. Fig. 2 (bottom panel) shows the 0th moment map of the field. The spectra are extracted within the CASA software and shown in Fig. B2. We also built a continuum image of aggregate bandwidth to check for possible detection of the galaxies in continuum. None of the objects are detected in the map with rms = 6 μJy, corresponding to a 5σ continuum flux limit of 30 μJy.

3.1.2 *Cosmological zoom-in simulations*

In order to reproduce the typical environment of $z \sim 0.3$ quasar absorbers, we turn to cosmological hydrosimulations. Our calculations are based on dedicated RAMSES ADAPTIVE MESH REFINEMENT (AMR) simulations with a total run time of 1.3 million CPU h (Frank et al. 2012). We zoomed on a region around the most massive halo with a box of size of ~ 14 Mpc h^{-1}. The higher level of refinement allows us to reach a spatial resolution of ~ 380 pc h^{-1} (comoving) at $z = 0$. In short, the simulations include non-thermal supernova feedback with 'on-the-fly' self-shielding option (Teyssier et al. 2013). With the goal of reproducing the expected surface brightness in the CGM regions of galaxies, we have post-processed the simulations taking into account gravitational cooling due to collisional ionization of accreting gas, photoionization by external UV sources and scattering from star-forming regions. Details of

[3] https://www.atnf.csiro.au/people/Matthew.Whiting/Duchamp/

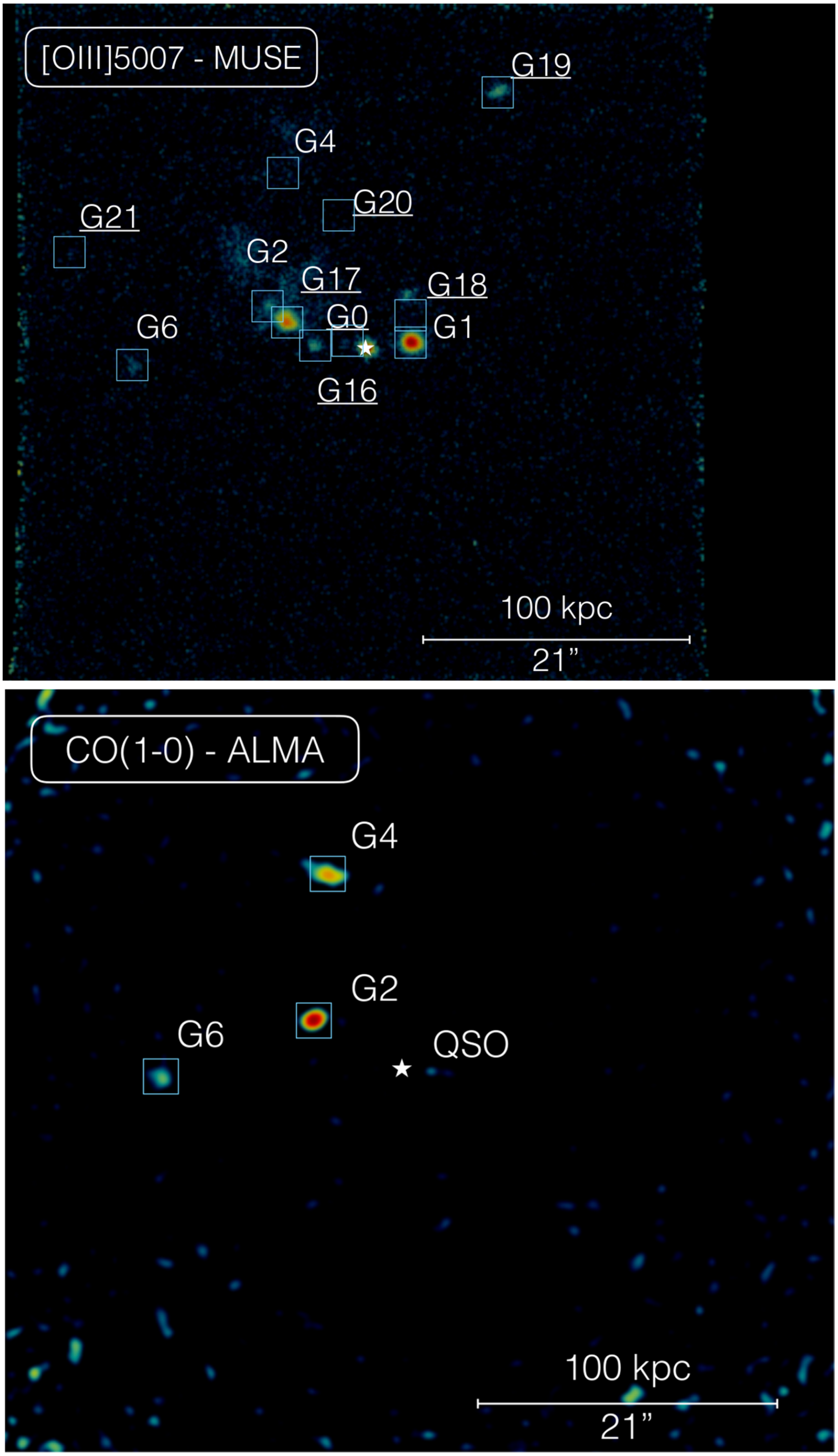

Figure 2. Galaxies at $z_{\rm abs} = 0.313$ in the field of Q1130−1449. *Top panel:* Continuum-subtracted MUSE pseudo-narrow-band filter around [O III] λ5007 at the redshift of the absorber. The quasar is shown as a white star and the positions of the galaxies are marked with light blue squares. Galaxies G4, G20, and G21 have no [O III] λ5007 emission lines but are detected in continuum. We report also low surface-brightness regions of diffuse gas around G2 and G4 showing all the prominent emission lines such as [O II], H β, [O III], H α, and [N II]. *Bottom panel:* ALMA Band 3 CO(1–0) 0th moment map of the same field on the same scale. We report three CO (1-0) emission detections matching MUSE galaxy positions (G2, G4, and G6).

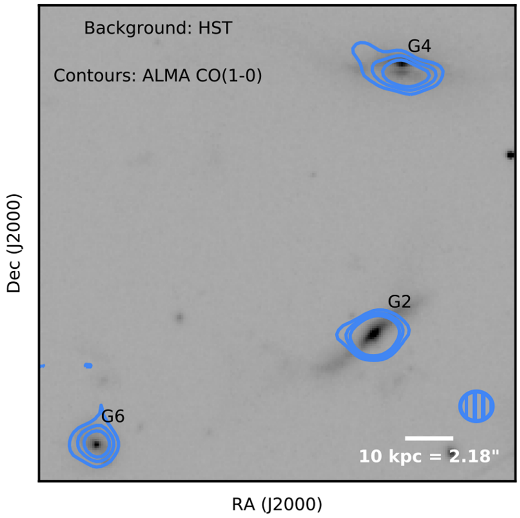

Figure 3. ALMA CO(1–0) contours overlaid on *HST* image. The contours show the –3, 3, 5, and 7σ levels, where the dashed negative contours above G6 reflect the noise level in the cube. The hatched ellipse shows the ALMA synthesized beam.

the simulation are presented in an upcoming paper (Augustin et al. submitted).

Current observations find that the SFR of strong-H I absorbers at $z \sim 0.3$ is just below 1 $M_{\odot}$ yr^{-1} (Rahmani et al. 2016), while their typical stellar masses are measured with values up to 10^{11} $M_{\odot}$ (Augustin et al. 2018) and their halo mass 10^{12} $M_{\odot}$ (Péroux et al. 2013). To best match these observable constraints, we picked a typical $z = 0.3$ halo in the zoom-in simulations which best mimics the properties of H I absorbers: an SFR = 1 $M_{\odot}$ yr^{-1}), $M_{star} = 10^{11}$ $M_{\odot}$, and $M_{DM} = 10^{12}$ $M_{\odot}$ ($R_{vir} = 200$ kpc h^{-1} comoving). Fig. 4 presents a MUSE-size field-of-view (FoV) Hα emission surface-brightness map of that simulated halo in units of erg s^{-1} cm^{-2} arcsec^{-2}. These simulations show the presence of multiple galaxies at the same redshift, typical of a small group. The group members have a broad range of masses so that some of these objects will remain undetected in current state-of-the-art observations. While the simulated objects appear more extended, the predicted surface brightness from the simulations are comparable to our Hα MUSE observations. The robustness of the surface brightness' prediction is a remarkable achievement which indicates that collisional and photoionization in combination can be the physical processes at the origin of the emission seen in the observations. In addition, this demonstrates that the brightest components of the CGM of low-redshift galaxies can be probed with current observations. Another important feature of the simulated cube is the presence of faint low surface-brightness gas with large sky cross-section in between galaxies.

3.1.3 The typical environment of low-redshift absorbers

Over the years, there has been mounting evidence that bright galaxies can be found at the redshift of quasar absorbers (see Krogager et al. 2017, for a recent review). Tremendous progress has come from IFU observations in particular which have provided a robust means to remove the bright quasar contamination and reach low impact parameters (Bouché et al. 2012; Péroux et al. 2012; Schroetter et al. 2016). At low redshifts, however, it is becoming clear that the picture is more complex than a simple one-to-one correspondence between a single galaxy and a quasar absorber. Thanks to the MUSE wide FoV, it is now possible to survey a large portion of sky in one observational set-up, with physical sizes (300 kpc across) typical of the CGM of galaxies (Steidel et al. 2010). Clearly, the case presented here does not contain the typical isolated galaxy-absorber match often reported in past searches for absorber counterparts. In part, this is due to deeper data as we are reaching limits of SFR > 0.01 $M_{\odot}$ yr^{-1}, i.e. an order of magnitude deeper than similar $z \sim 1$ studies. In addition, we report the detection of passive galaxies whose redshift estimate comes solely from Ca H&K absorption features and Balmer breaks detected in their continuum. While galaxies at these low redshifts will be more clustered, finding similar objects at higher redshifts is challenging as the continuum flux gets fainter.

While we note the possible alignments of the objects in what could be a filament with a north-west to south-east orientation (Møller & Fynbo 2001; Fumagalli et al. 2016; Péroux et al. 2017), it is also possible that these objects are part of a galaxy group. Assuming G2 as the central member galaxy, we note that G6, G4, G19, and G21 (lying to the north) are at velocity positions blueshifted with respect to G2 while G0, G16, and G17 (lying to the south) are redshifted with respect to G2. This alignment shows an overall direction of rotation in the halo of the group. The velocity dispersion of the system is $\sim$170 km s^{-1} which is in the range of small galaxy groups. Based on such dispersion and assuming a virialized spherical system, we obtain a virial radius of 420 kpc so that the MUSE FoV probes 1/3rd of the virial radius of the group. The virial mass for such system will be 2.9 $\times$ 10^{12} $M_{\odot}$. A number of studies have already reported several counterparts to low-redshift strong-H I absorbers (Bielby et al. 2017; Péroux et al. 2017; Borthakur et al. 2018; Klitsch et al. 2018; Rahmani et al. 2018a; Rahmani et al. 2018b; Klitsch et al. 2019) possibly tracing small groups.

In fact, these findings are in line with predictions from most recent numerical simulations of galaxy formation. At redshift $z = 3$, cosmological simulations have demonstrated the connection of quasar absorbers with large central haloes (Bird et al. 2014; Rahmati & Schaye 2014). The column densities observed also fall in the range expected from accretion occurring in the form of cold flows (Keres et al. 2005; Nelson et al. 2013). Similarly, galactic winds could produce some of this gas, where the most energetic systems will have the higher sky coverage. Recently, several groups have presented zoom-in hydrodynamical simulations which focus more resolution into the CGM regions to explore smaller physical scales (Hummels et al. 2019; Peeples et al. 2019; Suresh et al. 2019; van de Voort et al. 2019). The cosmological zoom-in simulations presented in Section 3.1.2 are specifically evolved to redshift zero with the goal to predict the emissivity of CGM gas around low-redshift galaxies thus enabling a more direct comparison with the observations presented here. They indicate that strong-H I absorbers could be associated with faint low surface-brightness intragroup gas. In the simulations, this gas is typically remnant tidal debris from previous interactions between the main galaxy and other smaller satellite galaxies. Indeed, the selection of absorbing systems on the basis of their sky coverage will favour interacting systems that have spread their gas around. The MUSE white light image (Fig. 1) shows clear indications of extended gas around G2 and G4 in particular.

This layout bears resemblance to cold gas streams similar to the Magellanic Stream (Richter et al. 2014). Low-redshift analogues of such groups include the M81 (NGC 3031)/M82 (NGC 3034)/NGC 3077 complex where optical observations tracing starlight indicate well-separated objects. 21 cm maps however show H I gas distributed in between these objects dominated by filamentary

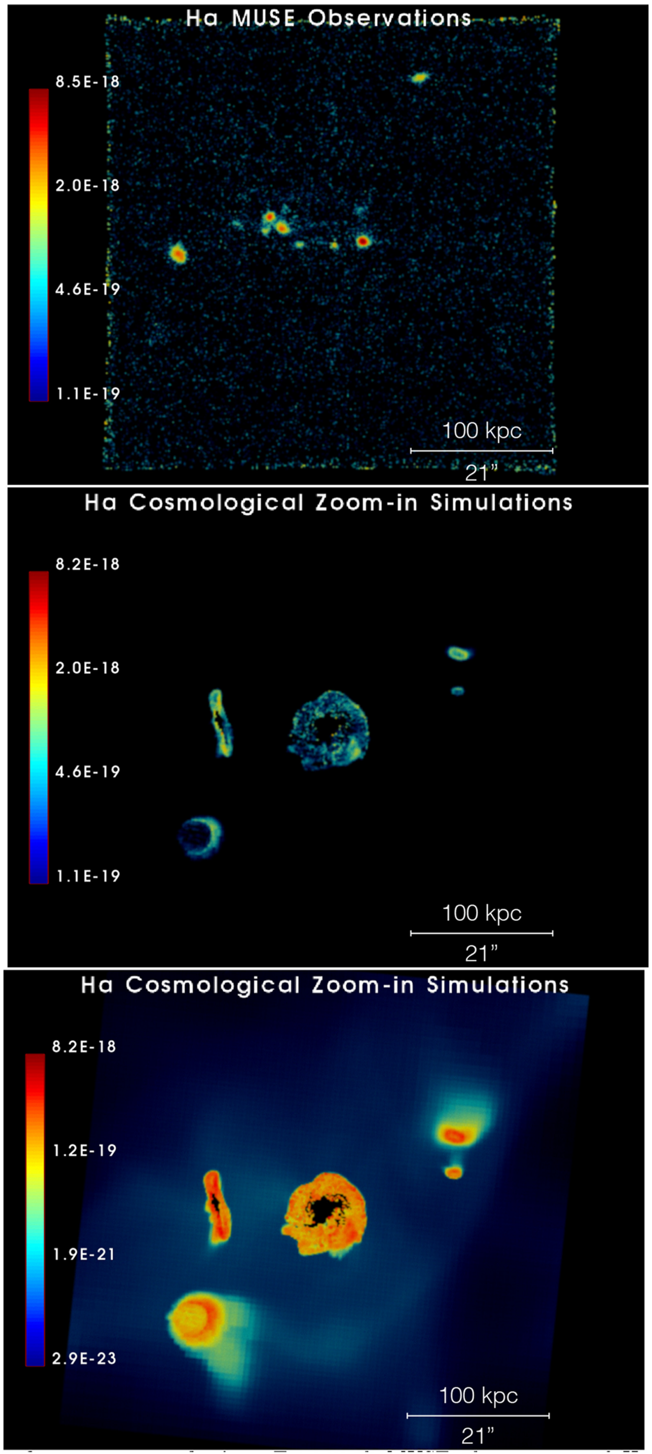

Figure 4. The environment of $z_{\rm abs} \sim 0.3$ galaxies. *Top panel:* MUSE observations of H α emission surface brightness (in erg s^{-1} cm^{-2} arcsec^{-2}) at $z = 0.313$ in the field of Q1130−1449. Every coloured object in this (continuum-subtracted) MUSE pseudo-narrow-band image indicates H α emission at the redshift of the absorber. *Middle panel:* RAMSES AMR cosmological zoom-in hydrodynamical simulations post-processed with photoionization models (Augustin et al., submitted). This MUSE-size field (1 × 1 arcmin, i.e. 300 kpc at $z = 0.313$) of H α emission surface brightness (in erg s^{-1} cm^{-2} arcsec^{-2}) shows a halo with an SFR, stellar, and halo masses typical of strong-H I quasar absorbers. The flux colour bar matches the MUSE observations. *Bottom panel:* Same figure with the minimum flux cut-off almost four orders of magnitude fainter than in the middle panel. The simulations show the presence of multiple galaxies at the same redshift with a broad range of masses as observed in the field of Q1130−1449. In addition, the predicted surface brightness from the simulations is comparable to our H α MUSE observations indicating that collisional and photoionization in combination can be the physical processes at the origin of the emission seen in the observations. These results demonstrate that the brightest components of the CGM of low-redshift galaxies can be probed with current observations of the emission, while the diffuse gas in between objects is at present best traced in absorption. These findings add to the paradigm shift where our former view of strong-N(H I) quasar absorbers being associated with a single bright galaxy changes towards a picture where the H I gas probed in absorption is related to far more complex galaxy structures.

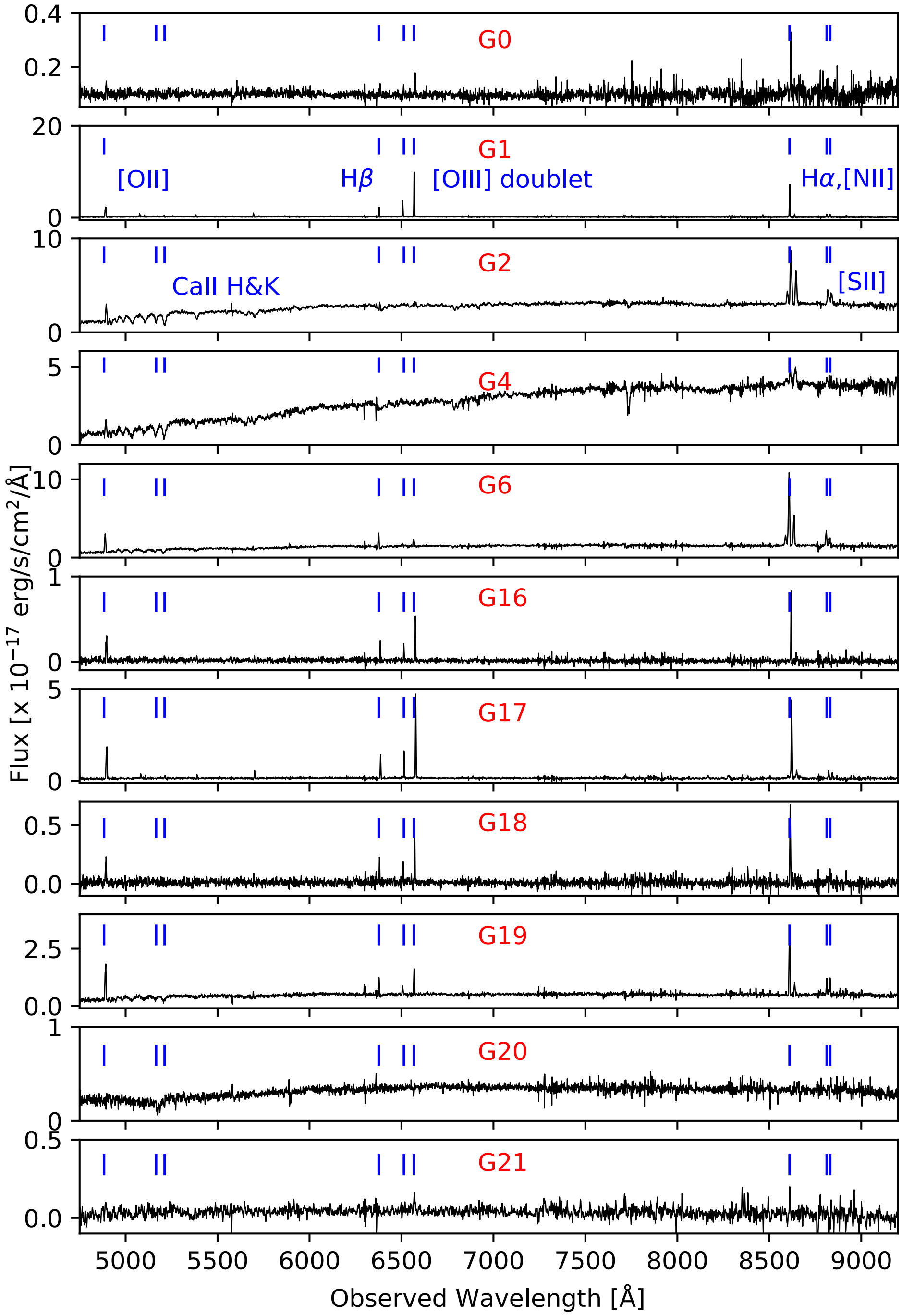

Figure 5. MUSE spectra of the galaxies at the redshift of the $\log[N(\text{H}\,\textsc{i})/\text{cm}^{-2}] = 21.71 \pm 0.07$ quasar absorber ($z_{\text{abs}} = 0.313$). The panels for G1 and G2 show key emission and absorption lines (at redshifted wavelengths), which lines can also be noted in galaxies plotted below. In some cases, no emission lines were detected, but strong Ca II absorption lines and a Balmer break matching $z_{\text{abs}} = 0.313$ were identified (e.g. G20). The spectrum of G21 is smoothed with a 3-pixel boxcar. In other cases, the galaxies have strong emission lines but faint continuum level (e.g. G0, G16, and G17) so that such objects would not appear in broad-band imaging. In particular, we discovered a faint galaxy closer to the quasar G0 at impact parameter $b = 2.3$ arcsec (10.6 kpc). While the object lies under the quasar PSF, several emission lines are clearly identified in the MUSE spectrum. In total, we report 11 objects at the redshift of the absorber in our MUSE data, 7 of which are new discoveries.

structures, clearly demonstrating the violent disruption of this system by tidal interaction (Yun, Ho & Lo 1993, 1994). Similarly, de Blok et al. (2014) report the detection of a cloud of neutral gas with admittedly lower column density outside the main H I disc of NGC 2403 which they argue could be either accreting from the intergalactic medium, or the result of a minor interaction with a neighbouring dwarf galaxy. Interestingly, they note that the velocities of the H I in NGC 2366 in the same group completely overlap with those of the H I in NGC 2403, which would make their absorption signature indistinguishable in the spectrum of a background object. 25 yr ago, Morris & van den Bergh (1994) had already calculated that the space density of Ly α absorbers and local

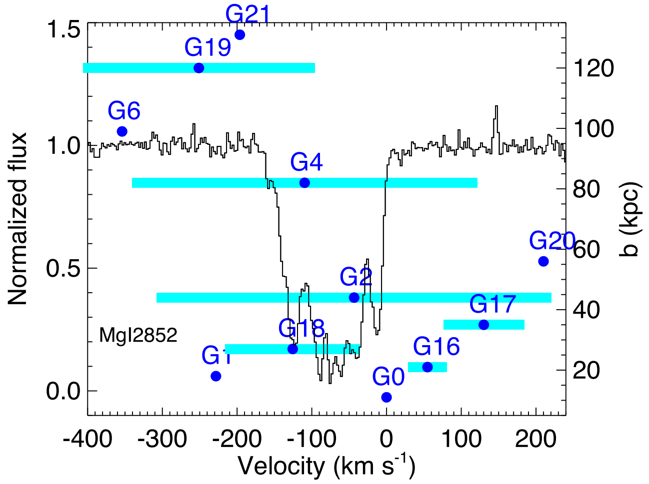

Figure 6. Impact parameters and velocities of galaxies relative to the quasar absorber profile. Normalized VLT/UVES quasar spectrum of Mg I 2852 line at z_{abs} = 0.31305. The systemic redshift of galaxy G0 is used as zero velocity reference. The galaxies are ordered from bottom to top as a function of impact parameter to the quasar line of sight (see right *y*-axis for values in kpc). The light blue horizontal lines indicate the V_{max} extent for galaxies exhibiting ordered rotation. The overlap in velocity space with the closest galaxies is somewhat limited, and much of the absorption bluewards of G0 could be related to the low surface-brightness tidal gas predicted in our simulations to be four orders of magnitude below the current detection threshold.

small groups matched, thus proposing that quasar absorbers can be produced by tidal debris in groups of galaxies.

These results pose a new challenge to the interpretation of the neutral gas probed in absorption. Indeed, most studies of the absorbing galaxies have concentrated on the brightest objects which are likely to be the main group member. Others have reasonably argued that the absorption is likely to arise from the galaxy with the smallest impact parameter to the quasar line of sight. Indeed, we note that lower mass galaxies such as G0 revealed here by the new MUSE observations of Q1130−1449 are expected to be one of the main contributors to galactic winds, given that the gas can more easily escape the galaxies' smaller potential wells. Fig. 6 shows the galaxies' positions with respect to the absorption profile in velocity space. The galaxies are ordered from bottom to top as a function of impact parameter to the quasar line of sight (see right *y*-axis for values in kpc). The light blue horizontal lines indicate the V_{max} extent for galaxies indicating rotation. The overlap in velocity space with the closest galaxies is somewhat limited, and much of the absorption bluewards of G0 could be related to the low surface-brightness tidal gas predicted in our simulations to be four orders of magnitude below the current detection threshold. These results strengthen previous reports of low-redshift strong-H I absorbers associated with groups (Bielby et al. 2017; Péroux et al. 2017; Borthakur et al. 2018; Klitsch et al. 2018; Rahmani et al. 2018a; Rahmani et al. 2018b; Klitsch et al. 2019). Altogether, these findings add to the paradigm shift where our former view of strong-*N*(H I) quasar absorbers being associated with a single bright galaxy changes towards a picture where the H I gas probed in absorption is related to far more complex galaxy structures. Since both winds and interactions are predicted to be enhanced in the distant Universe, these factors will likely become more important at higher redshifts but harder to discern.

3.2 Physical properties of the galaxy group

The MUSE observations provide a wealth of information on the stellar properties of the galaxies in the group. The MUSE galaxies spectra are displayed in Fig. 5 .Accurate redshifts are determined from multiple lines detected in the 1D MUSE spectra calibrated in air. We measured the emission fluxes from a Gaussian fit to the nebular lines. The 3σ upper limits for non-detection are computed for an unresolved source spread over 6 spatial pixels and spectral FWHM = 2.4 pixels = 3 Å. We followed the method described in Péroux et al. (2014) based on H α and H β to estimate moderate $E(B-V)$ and further correct the observed fluxes for dust attenuation. The resulting fluxes are tabulated in Table 1. The SFR with 1σ uncertainties were estimated from these H α fluxes following the relation of Kennicutt (1998). The emission line galaxies have values of SFR ranging from 0.1 to a few solar masses per year (see Table 2).

Following the methodology of Péroux et al. (2017), the H II region metallicities were measured from the strong-line indices (N2, O3N2, and R_{23} most relevant branch) following prescription by Kobulnicky, Kennicutt & Pizagno (1999) and the mean value of each of these was computed. Our estimates agreed within the errors with earlier measurements of G2 and G6 metallicities by Kacprzak et al. (2010). The metallicity of the galaxies in the group ranges from [X/H] = −0.57 ± 0.17 to 0.09 ± 0.16. The total metallicity of the neutral gas probed in absorption, [Zn/H] = −0.80 ± 0.16, is therefore consistent within the error bars with the lowest of the metallicities found in the galaxies in the MUSE image.

While metallicity gradients in galaxies could partly reconcile these measurements (Carton et al. 2018), we note that the low dust-corrected abundances measured in absorption resemble the properties of the extragalactic diffuse gas produced in our numerical simulations. Furthermore, the nebular emission line ratios place all but one galaxy into the star-forming region of the BPT diagram (Baldwin, Phillips & Terlevich 1981). Galaxy G1 shows evidence for ionization by an active galactic nucleus (AGN) with [O III]/H β = 5.45 and [N II]/H α = 0.07. The galaxy emission properties are listed in Table 2.

We used the ALMA observations to constrain the molecular gas content of the galaxy group. We measured the flux density in the lines by integrating the CO(1–0) emission lines in the extracted spectra (Fig. B2). We then computed the corresponding luminosities using the following formula: $L_{CO} = (3.25 \times 10^7 \times dL\ [Mpc]^2 \times F_{int}) / (f_{obs}\ [GHz]^2 \times (1 + z)^3)$, where dL is the luminosity distance, F_{int} the flux density, and f_{obs} = 87.8GHz is the observed frequency (Solomon, Downes & Radford 1992). Because we observe the CO(1–0) transition directly, our data naturally overcome uncertainties related to unknown CO line ratios. Estimates of the corresponding H_2 molecular masses however rely on the rather uncertain CO–H_2 conversion factor (Bolatto, Wolfire & Leroy 2013). Previous works have used Galactic CO–H_2 conversion factor of $\alpha_{CO} = 4.6\ M_{\odot}\ (K\ km\ s^{-1}\ pc^2)^{-1}$. Recent results by Klitsch et al. (2019) find that this is not always appropriate for absorbing galaxies so that here we opt to express the molecular masses as a function of α_{CO}. The resulting molecular masses range from M_{mol} = (1.00 ± 0.05) to (3.16 ± 0.07) × (α_{CO}/1 K km s^{-1} pc^2) × 10^9 $M_{\odot}$ and are listed Table 3.

The ALMA observations indicate substantial cold gas reservoirs in three of the galaxies in the group. These molecular masses are large in comparison with the typical stellar mass of absorbing galaxies (Augustin et al. 2018). In fact, a number of recent works have reported CO associated with quasar absorbers from ALMA observations with a high rate of incidence and derived equally

Table 1. Dust-corrected nebular emission line fluxes. The fluxes are expressed in units of erg s^{-1} cm^{-2}. The quoted errors are 1σ uncertainties. Galaxies G1 to G6 (shown in italics) were previously identified, while all the remaining are new identifications.

Galaxy	F([O II])	F(H β)	F([O III])	F([O III])	F(H α)	F([N II])
G0	1.6 ± 0.4	0.7 ± 0.2	1.0 ± 0.25	1.6 ± 0.4	4.5 ± 1.2	1.9 ± 0.5
G1	63.7 ± 15.9	40.6 ± 10.1	73.5 ± 18.4	221.4 ± 55.3	240.9 ± 60.2	17.3 ± 4.3
G2[a]	11.7 ± 2.9	3.9 ± 1.0	<0.9	2.2 ± 0.5	76.4 ± 19.1	53.1 ± 13.3
G4[a]	<23.5	<4.4	<5.0	<5.0	31.0 ± 7.7	–
G6[a]	27.8 ± 31.9	19.3 ± 4.8	3.5 ± 0.9	12.1 ± 3.0	200.6 ± 50.1	83.2 ± 20.8
G16	9.6 ± 2.4	3.9 ± 1.0	3.3 ± 0.8	10.4 ± 2.6	23.5 ± 5.9	1.5 ± 0.4
G17	70.9 ± 17.7	35.3 ± 8.8	42.8 ± 10.7	135.7 ± 38.4	200.4 ± 50.1	22.1 ± 5.5
G18	6.8 ± 1.7	3.5 ± 0.9	2.4 ± 0.6	9.7 ± 2.4	21.7 ± 5.4	3.8 ± 0.9
G19	25.6 ± 6.4	9.2 ± 2.3	6.0 ± 1.5	16.7 ± 4.2	72.0 ± 18.0	12.5 ± 3.1
G20[b]	<0.4	<0.2	<0.2	<0.2	<0.3	<0.3
G21[b]	<0.4	<0.3	<0.3	0.7 ± 0.2	0.7 ± 0.2	<0.7

Note. [a]Galaxies showing NaID absorption features in their spectra.
[b]The flux limits are not corrected for dust.

Table 2. Ionized gas properties of the galaxies detected at the redshift of the $z_{\rm abs} = 0.313$ absorber in the MUSE observations. We use the numbering system introduced by Kacprzak et al. (2010) when relevant and extend it for the seven new detections. δ is the angular distance from the quasar in arcsec and b is the impact parameter in kpc. SFR estimates are dust corrected. G20 and G21 have no or weak emission lines. Galaxies G1 to G6 (shown in italics) were previously identified.

Galaxy	RA	Dec.	δ (arcsec)	b (kpc)	$z_{\rm gal}$	$E(B-V)$ (mag)	SFR (M$_\odot$ yr^{-1})	12 + log(O/H)
G0	11 30 07.16	−14 49 27.13	2.3	10.6	0.31305	0.143	0.1 ± 0.1	8.58 ± 0.14
G1	11 30 06.74	−14 49 27.33	3.8	17.6	0.31205	0.098	3.4 ± 0.8	8.10 ± 0.08
G2	11 30 07.63	−14 49 23.93	9.5	43.9	0.31286	0.595	1.1 ± 0.3	8.73 ± 0.05
G4	11 30 07.54	−14 49 11.93	17.7	81.8	0.31257	>0.171	>0.4	<8.65[b]
G6	11 30 08.48	−14 49 29.13	21.3	98.5	0.31150	0.330	2.9 ± 0.7	8.75 ± 0.16
G16	11 30 07.34	−14 49 27.73	4.5	20.8	0.31329	0.099	0.3 ± 0.1	8.12 ± 0.14
G17	11 30 07.52	−14 49 25.13	7.6	35.1	0.31362	0.079	2.8 ± 0.7	8.09 ± 0.17
G18	11 30 06.77	−14 49 22.93	5.9	27.3	0.31250	0.111	0.3 ± 0.1	8.49 ± 0.18
G19	11 30 06.21	−14 49 04.53	26.0	120.2	0.31195	0.214	1.0 ± 0.2	8.50 ± 0.16
G20	11 30 07.20	−14 49 15.93	12.1	55.9	0.31397[a]	–	<0.01	–
G21	11 30 08.88	−14 49 19.13	28.4	131.3	0.31219	–	0.01 ± 0.01	8.56 ± 0.17[b]

Note. [a]Redshift based on Ca II absorption features in the galaxy spectrum. [b]Metallicity based on N2 indicator only.

Table 3. CO emitters at $z_{\rm abs} = 0.313$ in the ALMA observations. Flux densities, velocity widths, CO luminosities, molecular masses expressed in units of $\alpha_{\rm CO}$, and depletion time-scales are provided for each detected galaxy.

Galaxy	RA	Dec.	δ (arcsec)	b (kpc)	S$_{\rm CO}$ (Jy km s^{-1})	FWHM (km s^{-1})	L$_{\rm CO}$ (K km s^{-1} pc^2)	M$_{\rm mol}$ × ($\alpha_{\rm CO}$/1 K km s^{-1} pc^2) (× 10^9 M$_\odot$)	$\tau_{\rm depl}$ (Gyr)
G2	11 30 07.66	−14 49 23.41	9.7	44.8	0.63 ± 0.01	250 ± 50	(3.1 ± 0.1) × 10^9	3.16 ± 0.07	13 ± 5
G4	11 30 07.62	−14 49 11.44	18.0	83.2	0.42 ± 0.03	535 ± 50	(2.1 ± 0.1) × 10^9	1.99 ± 0.15	<23
G6	11 30 08.53	−14 49 28.54	21.5	99.4	0.20 ± 0.01	205 ± 50	(1.0 ± 0.1) × 10^9	1.00 ± 0.05	1.5 ± 0.5

high molecular masses (Neeleman et al. 2016; D'Odorico et al. 2018; Kanekar et al. 2018; Klitsch et al. 2018; Møller et al. 2018; Neeleman et al. 2018; Klitsch et al. 2019). However, it is unclear why H I-rich absorbing galaxies should have large reservoir of H_2 gas. At first sight, this might appear at odds with searches for H_2 rotational and vibrational transitions at UV rest-frame wavelengths which have only reported both low incident rates (10 per cent) and low molecular gas content ($f_{\rm mol} \leq 0.01$) with respect to the neutral gas (Ledoux, Petitjean & Srianand 2003; Noterdaeme et al. 2008). While the most abundant molecule after H_2, CO is known to be less abundant with a CO/H_2 column density ratio ranging from 10^{-7} to 10^{-5} and a mean value of 3×10^{-6} (Burgh et al. 2007). However, it must be borne in mind that the neutral atomic phase of the gas traces significantly lower gas densities than the molecular gas traced by CO (Snow & McCall 2006). Indeed the observations of nearby galaxies indicate that H I and H_2 are not co-spatial (Schruba et al. 2011), with the molecular gas concentrated in the central part of galaxies so that the detection of H_2 in absorption at an impact parameter distance at the edges of galaxies is less likely (Zwaan & Prochaska 2006; Obreschkow & Rawlings 2009).

In the field of Q1130−1449, we detected three objects in CO at the absorber redshift, two of which have large impact parameters ($b > 50$ kpc). The objects close to the quasar (i.e. G0 and G1) do not show CO(1–0) emission, although G1 is the most actively star-forming member of the group. We calculated the molecular depletion times for the three objects detected with ALMA following: $\tau_{\rm depl}$ = M_{H2}/SFR = 1/SFE, where SFE is the star formation efficiency. To compute the depletion time-scale, we assumed a Galactic CO–H_2 conversion factor of $\alpha_{\rm CO} = 4.6$ $M_\odot$ (K km s^{-1} pc^2)$^{-1}$. We derive $\tau_{\rm depl}$ ranging from 1.7 ± 0.5 to 12 ± 5 Gyr (see Table 3). The gas depletion times are long compared to the time-scales of the processes driving the evolution of the interstellar medium state (Leroy et al. 2013). Semenov, Kravtsov & Gnedin (2017) argue that star-forming gas converts only a small fraction (∼1 per cent) of its mass into stars while most of it (∼90 per cent) is dispersed by dynamical and feedback processes. Selection based on strong-H I absorbers thus possibly preferentially finds galaxies with large molecular gas reservoirs (at given SFR) which inefficiently convert their gas into stars (Kanekar et al. 2018).

3.3 Morphological and kinematical properties of group members

MUSE and ALMA observations of the field are also complementary in that they both provide information on the kinematics of the stars and molecular gas respectively. We performed a three-dimensional morpho-kinematic analysis of the objects detected in MUSE and ALMA, using the method described in Péroux et al. (2017). In brief, we used the GALPAK$^{\rm 3D}$ algorithm (Bouché et al. 2015) which compares directly the data cube with a parametric model mapped in x, y, and λ coordinates. The algorithm uses a Markov Chain Monte Carlo (MCMC) approach with a proposed distribution of the parameters in order to efficiently probe the parameter space. The code has the advantages that it fits the galaxy in 3D space and provides a robust description of the morpho-kinematics of the data. We assessed the quality of the fit from a χ^2 minimization as well as the inspection of the residual maps. We mostly used the brightest [O III] 5007 Å line to perform the analysis. Our results are tabulated in Table 4 and illustrated in Figs B1 and B2 in Appendix B for the MUSE and ALMA detections, respectively. The CO velocity fields are well resolved in our ALMA observations. As expected, the stellar sizes as measured by $r_{1/2}$ are larger than the molecular gas sizes. Our analysis further provides a determination of the inclination and position angle (PA) of the galaxies. In cases where GALPAK$^{\rm 3D}$ did not converge (namely for G0, G1, G6, G20, and G21), we use SEXTRACTOR to derive these parameters from the broad-band *HST*/WFPC2 image.

The analysis of galaxy G0 is hampered by the proximity to the bright quasar (2.3 arcsec). G1 shows no indication of a velocity shear notwithstanding the bright emission lines in the object and a favourable inclination parameter (i = 51 deg) as measured in the *HST*/WFPC2 broad-band image. Indeed, the nebular emission line ratios in the object show evidence for ionization by an AGN with H α emission produced in the central engine (Baldwin et al. 1981). G2 is a large galaxy (half-light radius $r_{1/2}$ = 14 ± 2 kpc) dominated by rotation in both [O III] and CO as indicated by the dispersion velocity for G2 peaking in the centre of the system beyond beam smearing. A smaller nearby galaxy, G17, presumably interacts with this system. The MUSE white light image (Fig. 1) also shows extended gas around the galaxy. For galaxy G4, we used the H α emission line rather than the fainter [O III] 5007 Å. The ALMA observations of G4 indicate two, spectrally and spatially well-separated components (Fig. 3) clearly seen in the spectrum (Fig. B2) with wide FWHM = 530 ± 50 km s^{-1}. This is reflected in the kinematics analysis where we derive a large $V_{\rm max}$ = 290 ± 4 km s^{-1} for this system. We tentatively interpret these characteristics as a signature of merging and note extended diffuse gas is also present in the MUSE white light image (Fig. B1). Galaxy G6 is almost face-on (i = 18 deg) hindering the kinematical analysis of this system. An inspection of the velocity field of G16 reveals that it has yet to converge to its $V_{\rm max}$ value, which should be taken as an upper limit. The faint galaxy G17 on the other hand has a well-converged velocity field as illustrated in Fig. B1. Our detection of galaxy G19 indicates that our observations have not fully reached $V_{\rm max}$ either, although rotation can be securely reported. Galaxy G20 is a continuum-detected object while G21 has faint emission lines thus precluding further kinematic analysis. Overall, the model converges for most galaxies. While not a unique solution, these findings indicate that the emission lines are well described by disc rotation. However, such an analysis might be rather insensitive to interactions of large objects with lower mass galaxies (say, as in the case of G2 and G17).

We derived the dynamical mass of each galaxy from the enclosed mass: $M_{\rm dyn} = V_{\rm max}^2\, r_{1/2} / G$ (Péroux et al. 2011b). Assuming a spherical virialized collapse model (Mo & White 2002), we further computed the halo mass related to each object: $M_{\rm halo} = 0.1 H_{\rm o}^{-1} G^{-1} \Omega_{\rm m}^{-0.5} (1+z)^{-1.5} V_{\rm max}^3$. The highest of these values are representative within the errors of our estimate of the halo mass of the whole group (log $M_{\rm halo}$ = 12.5 $M_\odot$). For one of these objects (G1), Christensen et al. (2014) performed a Spectral Energy Distribution (SED) fit to the optical and near-infrared magnitudes and derived a low stellar mass of log $M_* = 8.29 \pm 0.09$ $M_\odot$.

When an object is detected from its nebular emission lines and in CO(1–0), i.e. G2, G4, and G6, both the ionized gas traced by nebular lines and the CO molecular line widths (FWHM = 200–530 km s^{-1}) are significantly broader than the neutral gas traced by absorption at some distance from the galaxies (∼150 km s^{-1}) and especially the 21cm line absorption (FWHM = 42.1 ± 2.7 km s^{-1}). The kinematics of the stars and molecular gas in terms of orientation (PA) deviate by 7σ (G2) or rather similar (G4). The maximum velocities differ significantly: 264 ± 3 km s^{-1} (H α) versus 134 ± 2 km s^{-1} (CO) for G2 and 231 ± 4 km s^{-1} (H α) versus 290 ± 4 km s^{-1} (CO) for G4. Levy et al. (2018) made a detailed comparison of the molecular and ionized gas (traced by H α) kinematics in a sample of local galaxies. They find that ∼75 per cent of their sample galaxies have smaller ionized gas rotation velocities than the molecular gas in the outer part of the rotation curve. They report no case where the molecular gas rotation velocity is measurably lower than that of the ionized gas unlike what we observe in the case of galaxy G2.

4 CONCLUSION

In this paper, we have presented deep MUSE and ALMA observations of the field of the QSO Q1130−1449 which shows a log [N(H I)/cm^{-2}] = 21.71 ± 0.07 damped Ly α system at $z_{\rm abs} = 0.313$. Our main findings can be summarized as follow:

(i) Our MUSE observations cover 11 galaxies at the redshift of the absorber, 7 of which are new discoveries. In particular, we report a new object with the smallest impact parameter to the quasar line of sight (b = 10.6 kpc). Three of the objects are also detected in CO(1–0) in our ALMA observations.

Table 4. Nebular emission lines and cold molecular gas (bold) morpho-kinematic properties. The results of the three-dimensional MCMC forward modelling of the morphological and kinematical parameters listed are all inclination corrected. Inclination and PA (NoE) are derived from a SEXTRACTOR fit to the broad-band *HST*/WFPC2 image when the algorithm did not converge. When the object is detected in both MUSE and ALMA, i.e. G2, G4, and G6, the kinematic models (bold) are sometimes found to be in good agreement indicating a relation between the stellar content and the molecular gas in some of these galaxies. The maximum velocity of the discs are used to derive the dynamical and halo masses. Galaxies G1 to G6 (shown in italics) were previously identified.

	$r_{1/2}$ (kpc)	i (deg)	PA (deg)	$V_{\rm max}$ (km s^{-1})	log $M_{\rm dyn}$ (M$_\odot$)	log $M_{\rm halo}$ (M$_\odot$)
G0	under quasar PSF	67	122	–	–	–
G1	dispersion dominated	51	91	–	–	–
G2	14 ± 2	77 ± 2	131 ± 2	264 ± 14	11.3 ± 0.2	12.9 ± 0.1
G2	2 ± 1	76 ± 3	117 ± 2	134 ± 14	–	–
G4	9 ± 2	54 ± 2	86 ± 2	231 ± 12	11.1 ± 0.2	12.7 ± 0.1
G4	6 ± 1	82 ± 4	84 ± 2	290 ± 19	–	–
G6	face-on	18	33	–	–	–
G6	face-on	–	–	–	–	–
G16	3 ± 2	33 ± 25	66 ± 33	<26	<8.7	<9.8
G17	3 ± 1	52 ± 1	54 ± 1	54 ± 13	9.4 ± 0.3	10.8 ± 0.1
G18	5 ± 1	32 ± 10	103 ± 11	90 ± 34	9.4 ± 0.9	11.5 ± 0.4
G19	3 ± 1	63 ± 4	110 ± 4	155 ± 68	10.3 ± 0.5	12.2 ± 0.3
G20	continuum-detected	10	130	–	–	–
G21	faint emission lines	28	147	–	–	–

(ii) Using dedicated numerical cosmological simulations, we infer that the physical properties of these galaxies qualitatively resemble a small group environment, possibly part of a filamentary structure.

(iii) Based on metallicity and velocity arguments, we conclude that the neutral gas traced by strong-H I absorbers is only partly related to these emitting galaxies while a larger fraction is likely the signature of low surface brightness emitting gas four orders of magnitude fainter than the current detection limits outside the Local Group.

(iv) We report large molecular gas reservoirs with long depletion time-scales in the three galaxies detected with ALMA. These results together with other reports of large molecular masses in strong-H I absorption systems indicate that selection based on absorption preferentially picks galaxies which inefficiently convert their gas into stars.

(v) Detailed kinematics analysis of both the ionized and molecular component of these galaxies shows signatures of past interactions and possible merging between various members of the group. While the stellar component is spatially more extended, the resolved molecular lines are broader in velocity space.

(vi) Together with other similar reports, our findings challenge a picture where strong-N(H I) quasar absorbers are associated with a single bright galaxy and favour a scenario where the H I gas probed in absorption is related to far more complex galaxy structures.

ACKNOWLEDGEMENTS

We thank Thomas Ott, Nicolas Bouché and Jean-Charles Lambert for developing and distributing the QFITSVIEW, GALPAK$^{\rm 3D}$, and GLNEMO software, respectively. We thank Chian-Chou Chen (TC) for help with the CO column density calculation. The authors wish to thank the anonymous referee for insightful comments which have led to significant improvement in the quality of the manuscript.

CP thanks the Alexander von Humboldt Foundation for the granting of a Bessel Research Award held at MPA. CP is also grateful to the ESO and the DFG cluster of excellence 'Origin and Structure of the Universe' for support. AK acknowledges STFC grant ST/P000541/1 and Durham University. RA thanks CNRS and CNES (Centre National d'Etudes Spatiales) for support for her PhD. VPK acknowledges partial support from NASA grant NNX14AG74G and NASA/Space Telescope Science Institute support for *Hubble Space Telescope* programs GO-13733 and 13801. LAS acknowledges support from ERC Grant agreement 278594-GasAroundGalaxies. This work has been carried out thanks to the support of the OCEVU Labex (ANR-11-LABX-0060) and the A∗MIDEX project (ANR-11-IDEX-0001-02) funded by the 'Investissements d'Avenir' French government program managed by the ANR.

We are grateful to the Paranal and Garching staff at ESO for performing the observations in service mode and the instrument team for making a reliable instrument. This paper makes use of the following ALMA data: ADS/JAO.ALMA#2016.1.01250.S. ALMA is a partnership of ESO (representing its member states), NSF (USA) and NINS (Japan), together with NRC (Canada), NSC and ASIAA (Taiwan), and KASI (Republic of Korea), in cooperation with the Republic of Chile. The Joint ALMA Observatory is operated by ESO, AUI/NRAO and NAOJ.

Based on observations collected at the European Organisation for Astronomical Research in the Southern Hemisphere under ESO programme(s) 67.A-0567, 69.A-0371, and 096.A-0303.

REFERENCES

Anderson M. E., Bregman J. N., 2010, ApJ, 714, 320
Augustin R. et al., 2018, MNRAS, 478, 3120
Baldwin J. A., Phillips M. M., Terlevich R., 1981, PASP, 93, 5

Bechtold J., Siemiginowska A., Aldcroft T. L., Elvis M., Dobrzycki A., 2001, ApJ, 562, 133
Bergeron J., Boisse P., 1991, A&A, 234, 344
Bielby R., Crighton N. H. M., Fumagalli M., Morris S. L., Stott J. P., Tejos N., Cantalupo S., 2017, MNRAS, 468, 1373
Bielby R. M. et al., 2018, preprint(arXiv:1809.05544)
Bird S., Vogelsberger M., Haehnelt M., Sijacki D., Genel S., Torrey P., Springel V., Hernquist L., 2014, MNRAS, 445, 2313
Bolatto A. D., Wolfire M., Leroy A. K., 2013, ARA&A, 51, 207
Borthakur S., Momjian E., Heckman T. M., Catinella B., Vogt F. P. A., Tumlinson J., 2018, preprint(arXiv:1812.01632)
Bouché N. et al., 2012, MNRAS, 419, 2
Bouché N. et al., 2016, ApJ, 820, 121
Bouché N., Murphy M. T., Péroux C., Davies R., Eisenhauer F., Förster Schreiber N. M., Tacconi L., 2007, ApJ, 669, L5
Bouché N., Murphy M. T., Kacprzak G. G., Péroux C., Contini T., Martin C. L., Dessauges-Zavadsky M., 2013, Science, 341, 50
Bouché N., Carfantan H., Schroetter I., Michel-Dansac L., Contini T., 2015, Astrophysics Source Code Library, record ascl:1501.014
Bregman J. N., Anderson M. E., Miller M. J., Hodges-Kluck E., Dai X., Li J.-T., Li Y., Qu Z., 2018, ApJ, 862, 3
Burgh E. B., France K., McCandliss S. R., 2007, ApJ, 658, 446
Carton D. et al., 2018, MNRAS, 478, 4293
Christensen L., Møller P., Fynbo J. P. U., Zafar T., 2014, MNRAS, 445, 225
Chun M. R., Gharanfoli S., Kulkarni V. P., Takamiya M., 2006, AJ, 131, 686
D'Odorico V. et al., 2018, ApJ, 863, L29
de Blok W. J. G. et al., 2014, A&A, 569, A68
Deharveng J.-M., Buat V., Bergeron J., 1995, A&A, 298, 57
Frank S. et al., 2012, MNRAS, 420, 1731
Fumagalli M., Cantalupo S., Dekel A., Morris S. L., O'Meara J. M., Prochaska J. X., Theuns T., 2016, MNRAS, 462, 1978
Guber C. R., Richter P., Wendt M., 2018, A&A, 609, A85
Hummels C. B. et al., 2019, preprint(arXiv:1811.12410)
Husemann B., Bennert V. N., Scharwächter J., Woo J.-H., Choudhury O. S., 2016, MNRAS, 455, 1905
Joshi R., Srianand R., Petitjean P., Noterdaeme P., 2017, MNRAS, 471, 1910
Kacprzak G. G., Murphy M. T., Churchill C. W., 2010, MNRAS, 406, 445
Kanekar N. et al., 2014, MNRAS, 438, 2131
Kanekar N. et al., 2018, ApJ, 856, L23
Kanekar N., Smette A., Briggs F. H., Chengalur J. N., 2009, ApJ, 705, L40
Kennicutt R. C., 1998, ARA&A, 36, 189
Kereš D., Katz N., Weinberg D. H., Davé R., 2005, MNRAS, 363, 2
Klitsch A., Péroux C., Zwaan M. A., Smail I., Oteo I., Biggs A. D., Popping G., Swinbank A. M., 2018, MNRAS, 475, 492
Klitsch A. et al., 2019, MNRAS, 482, L65
Kobulnicky H. A., Kennicutt R. C., Pizagno J. L., 1999, ApJ, 514, 544
Krogager J.-K., Møller P., Fynbo J. P. U., Noterdaeme P., 2017, MNRAS, 469, 2959
Lane W., Smette A., Briggs F., Rao S., Turnshek D., Meylan G., 1998, AJ, 116, 26
Leclercq F. et al., 2017, A&A, 608, A8
Ledoux C., Petitjean P., Srianand R., 2003, MNRAS, 346, 209
Leroy A. K. et al., 2013, AJ, 146, 19
Levy R. C. et al., 2018, ApJ, 860, 92
Mangum J. G., Shirley Y. L., 2015, PASP, 127, 266
McGaugh S. S., 2008, in Davies J. I., Disney M. J., eds, Proc. IAU Symp. 244, Dark Galaxies and Lost Baryons. Kluwer, Dordrecht, p. 136
Morris S. L., van den Bergh S., 1994, ApJ, 427, 696
Morris S. L., Weymann R. J., Dressler A., McCarthy P. J., Smith B. A., Terrile R. J., Giovanelli R., Irwin M., 1993, ApJ, 419, 524
Mo H. J., White S. D. M., 2002, MNRAS, 336, 112
Møller P. et al., 2018, MNRAS, 474, 4039
Møller P., Fynbo J. U., 2001, A&A, 372, L57
Narayanan A., Misawa T., Charlton J. C., Kim T.-S., 2007, ApJ, 660, 1093
Neeleman M. et al., 2016, ApJ, 820, L39
Neeleman M., Kanekar N., Prochaska J. X., Christensen L., Dessauges-Zavadsky M., Fynbo J. P. U., Møller P., Zwaan M. A., 2018, ApJ, 856, L12
Nelson D., Vogelsberger M., Genel S., Sijacki D., Kereš D., Springel V., Hernquist L., 2013, MNRAS, 429, 3353
Nicastro F. et al., 2018, Nature, 558, 406
Noterdaeme P., Ledoux C., Petitjean P., Srianand R., 2008, A&A, 481, 327
Obreschkow D., Rawlings S., 2009, MNRAS, 394, 1857
Peeples M. S. et al., 2019, preprint(arXiv:1810.06566)
Péroux C. et al., 2017, MNRAS, 464, 2053
Péroux C., Bouché N., Kulkarni V., York D., Vladilo G., 2011a, MNRAS, 410, 2237
Péroux C., Bouché N., Kulkarni V., York D., Vladilo G., 2011b, MNRAS, 410, 2251
Péroux C., Bouché N., Kulkarni V. P., York D. G., Vladilo G., 2012, MNRAS, 419, 3060
Péroux C., Bouché N., Kulkarni V. P., York D. G., 2013, MNRAS, 436, 2650
Péroux C., Kulkarni V. P., York D. G., 2014, MNRAS, 437, 3144
Péroux C., Rahmani H., Arrigoni Battaia F., Augustin R., 2018, MNRAS, 479, L50
Piqueras L., Conseil S., Shepherd M., Bacon R., Leclercq F., Richard J., 2017, ADASS XXVI proceedings, preprint(arXiv:1710.03554)
Rahmani H. et al., 2016, MNRAS, 463, 980
Rahmani H. et al., 2018a, MNRAS, 474, 254
Rahmani H. et al., 2018b, MNRAS, 480, 5046
Rahmati A., Schaye J., 2014, MNRAS, 438, 529
Richter P., Fox A. J., Ben Bekhti N., Murphy M. T., Bomans D., Frank S., 2014, Astron. Nachr., 335, 92
Rudie G. C. et al., 2012, ApJ, 750, 67
Rudie G. C., Newman A. B., Murphy M. T., 2017, ApJ, 843, 98
Schroetter I. et al., 2016, ApJ, 833, 39
Schroetter I., Bouché N., Péroux C., Murphy M. T., Contini T., Finley H., 2015, ApJ, 804, 83
Schruba A. et al., 2011, AJ, 142, 37
Semenov V. A., Kravtsov A. V., Gnedin N. Y., 2017, ApJ, 845, 133
Skúladóttir Á., Salvadori S., Pettini M., Tolstoy E., Hill V., 2018, A&A, 615, A137
Snow T. P., McCall B. J., 2006, ARA&A, 44, 367
Solomon P. M., Downes D., Radford S. J. E., 1992, ApJ, 398, L29
Steidel C. C., Erb D. K., Shapley A. E., Pettini M., Reddy N., Bogosavljević M., Rudie G. C., Rakic O., 2010, ApJ, 717, 289
Straka L. A., Whichard Z. L., Kulkarni V. P., Bishof M., Bowen D., Khare P., York D. G., 2013, MNRAS, 436, 3200
Straka L. A. et al., 2015, MNRAS, 447, 3856
Suresh J., Nelson D., Genel S., Rubin K. H. R., Hernquist L., 2019, MNRAS, 483, 4040
Teyssier R., Pontzen A., Dubois Y., Read J. I., 2013, MNRAS, 429, 3068
Tripp T. M., Lu L., Savage B. D., 1998, ApJ, 508, 200
Turner M. L., Schaye J., Steidel C. C., Rudie G. C., Strom A. L., 2014, MNRAS, 445, 794
van de Voort F., Springel V., Mandelker N., van den Bosch F. C., Pakmor R., 2019, MNRAS, 482, L85
Weilbacher P., 2015, Science Operations 2015: Science Data Management. ESO/ESA Workshop, ESO Garching, p. 1
Werk J. K., Prochaska J. X., Thom C., Tumlinson J., Tripp T. M., O'Meara J. M., Peeples M. S., 2013, ApJS, 204, 17
Wisotzki L. et al., 2016, A&A, 587, A98
Wisotzki L. et al., 2018, Nature, 562, 229
York D. G. et al., 2012, MNRAS, 423, 3692
York D. G., Dopita M., Green R., Bechtold J., 1986, ApJ, 311, 610
Yun M. S., Ho P. T. P., Lo K. Y., 1993, ApJ, 411, L17
Yun M. S., Ho P. T. P., Lo K. Y., 1994, Nature, 372, 530
Zwaan M. A., Prochaska J. X., 2006, ApJ, 643, 675
Zwaan M. A., Liske J., Péroux C., Murphy M. T., Bouché N., Curran S. J., Biggs A. D., 2015, MNRAS, 453, 1268

APPENDIX A: GAS ABSORPTION PROFILES

We obtained the VLT/UVES reduced quasar spectra from the ESO advanced data products archives.[4] We applied a heliocentric cor-

[4] http://archive.eso.org/cms.html

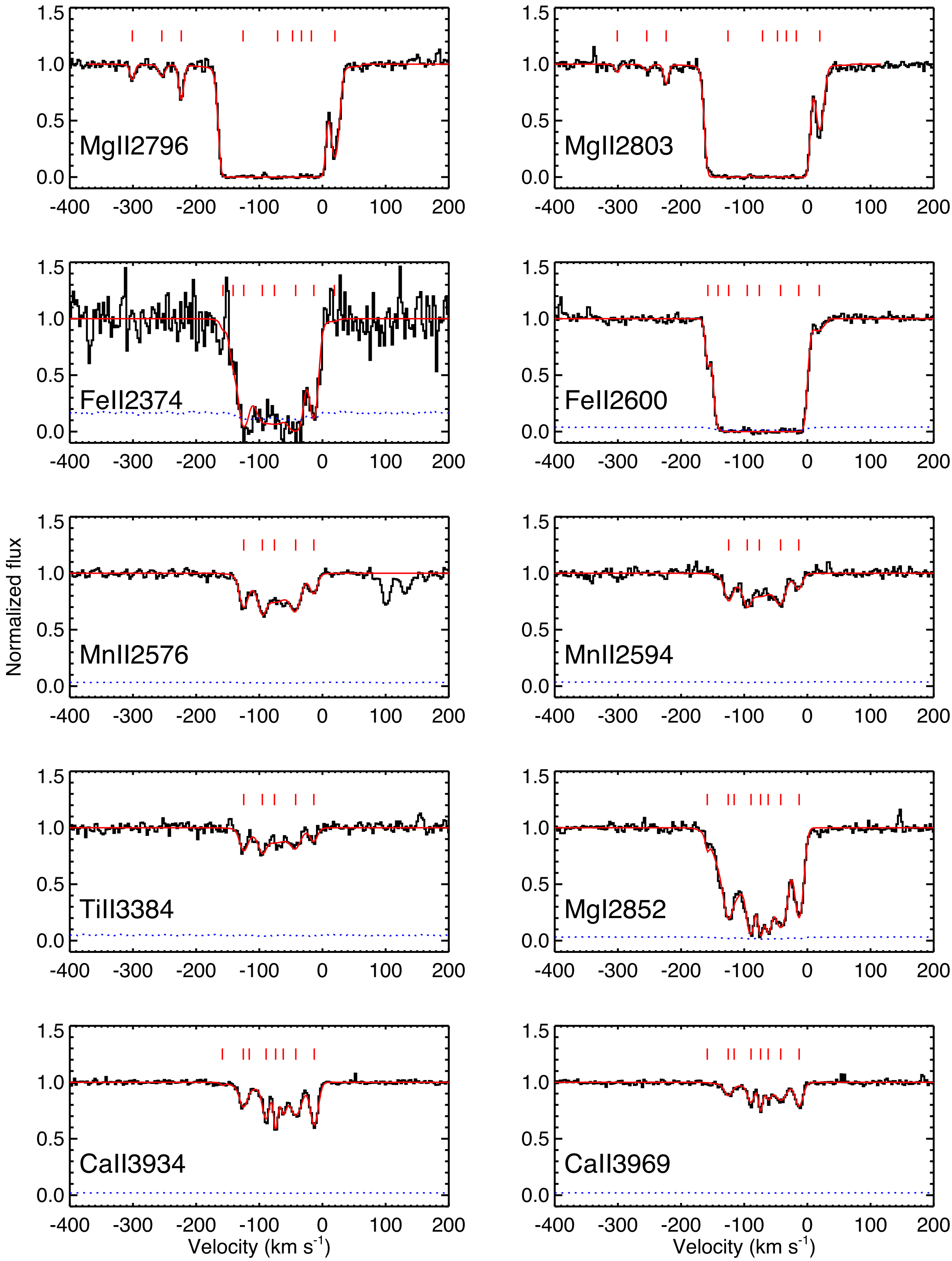

Figure A1. VLT/UVES normalized spectrum of quasar Q1130−1449. The zero velocity is set to the systemic redshift of galaxy G0 $z_{\rm gal}$ =0.31305. Most of the absorption lies bluewards of this systemic redshift. Voigt profile fits to the absorption profile are shown in red and the fitted components are shown as tick marks above the spectrum. The error array is shown as a dotted blue line. Mg II and Fe II lines are saturated, but a good fit could be obtained from weaker elements like Mn II, Ti II, and Ca II.

rection, combined the individual exposures weighting by SNR and normalized the combined quasar continuum. Fig. A1 shows portions of the VLT/UVES normalized spectrum of the quasar showing the metal absorption profiles where the zero velocity is set to the systemic redshift of galaxy G0, $z_{\rm gal}$ =0.31305. The profiles span a wide velocity range of $\sim$250 km s^{-1} with the weakest components at $-350 < v < -200$ km s^{-1} only seen in Mg II 2796 2803. We modelled the absorption lines with Voigt profiles using VPFIT[5] v10.0. The resulting metallicity derived from all Fe II, Mn II, and Ti II are consistent with each other leading to [X/H] = -1.94 ± 0.08 or 1 per cent solar. This is significantly lower than the measurement based on Zn from *HST*/STIS, [Zn/H]=-0.80 ± 0.16 (16 per cent solar). This would conventionally be explained by postulating a modest amount of dust along this line of sight, which would not affect Zn but only refractory elements such as Fe, Mn, Ti, and Ca. We note however recent work by Skúladóttir et al. (2018) who warn that stars in the Sculptor dwarf spheroidal galaxy indicate that Zn and Fe do not trace all the same nucleosynthetic production channels, so that a direct comparison might not be appropriate. It is also important to note that the [Zn/H] measurement is based on *HST*/STIS which have a significantly lower spectral resolution than the VLT/UVES spectrum studied here.

[5] http://www.ast.cam.ac.uk/rfc/vpfit.html

APPENDIX B: MORPHO-KINEMATICS ANALYSIS OF GALAXIES IN THE FIELD

The section displays the flux and velocity maps of individual galaxies observed at $z_{\rm gal} = 0.313$ with MUSE and ALMA.

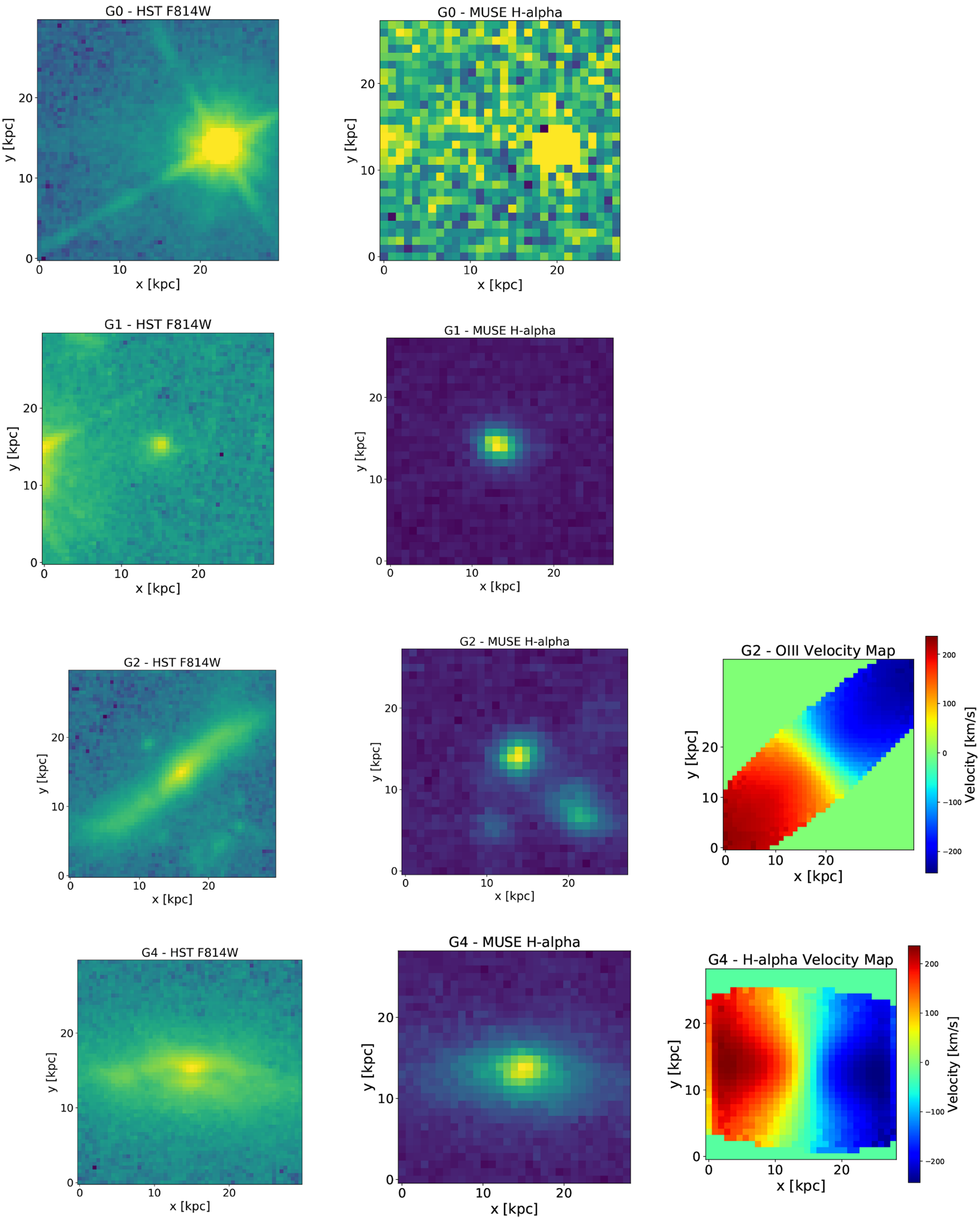

Figure B1. Gas content of individual galaxies detected in MUSE at $z_{\rm abs} = 0.313$. Postage stamps of the stellar continuum observed with *HST*/WFPC2 (left), nebular emission of [O III] or H α from MUSE narrow-band images (centre) and modelled velocity maps convolved with the instrumental PSF (right). North is up, east to the left. The signal in galaxy G0 panel is dominated by the bright nearby quasar (slightly off-centre to the West). While the object lies under the quasar PSF, several emission lines are clearly identified in the MUSE spectrum after quasar spectral-PSF subtraction (see Fig. 5). Some object are bright in continuum but have weak or undetected emission lines (e.g. G20) so that they are apparent in the *HST* data but weak in MUSE narrow band. Conversely, some objects show strong emission lines with faint continuum (e.g. G0 and G16).

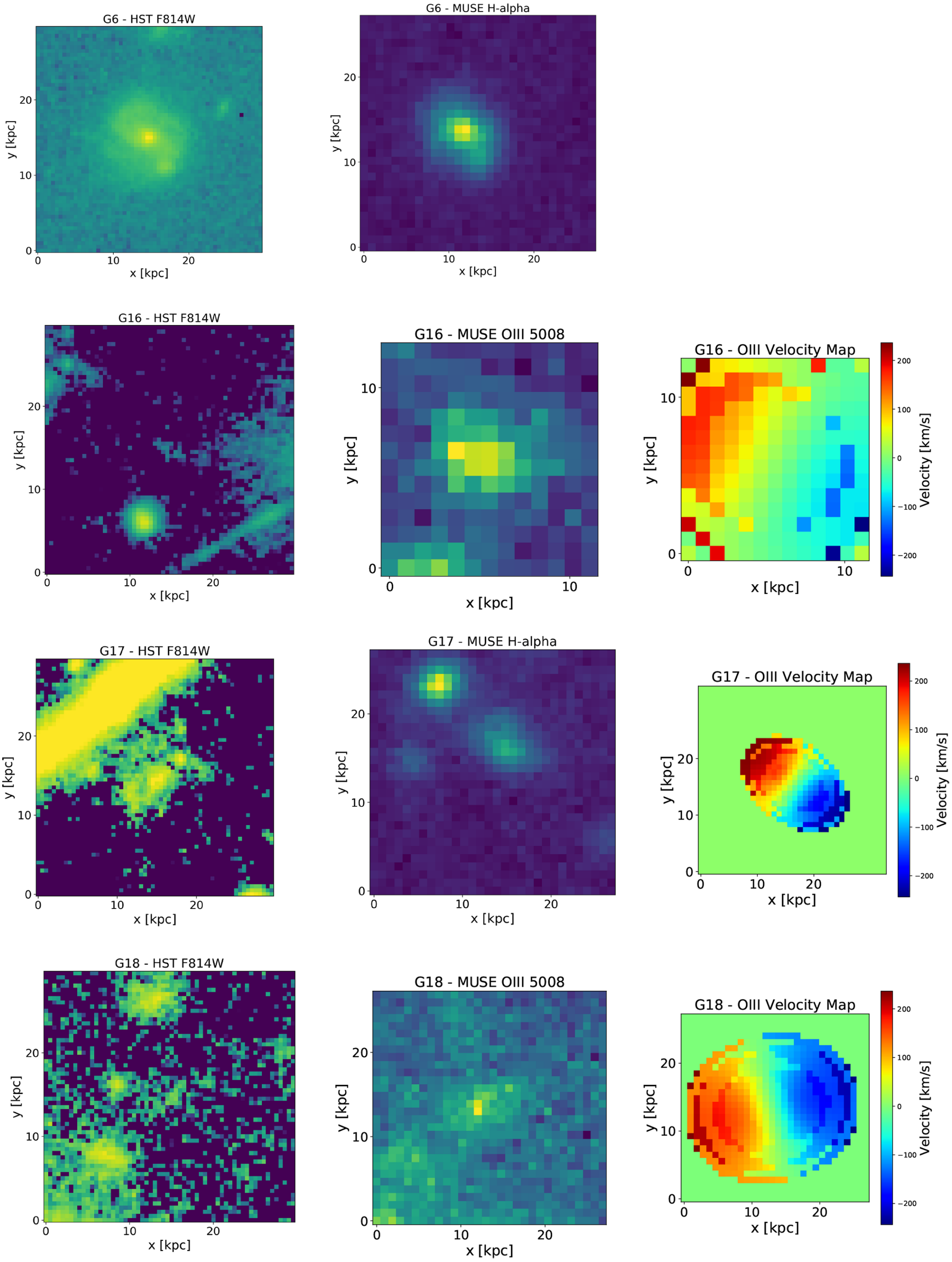

Figure B1 – *Continued*

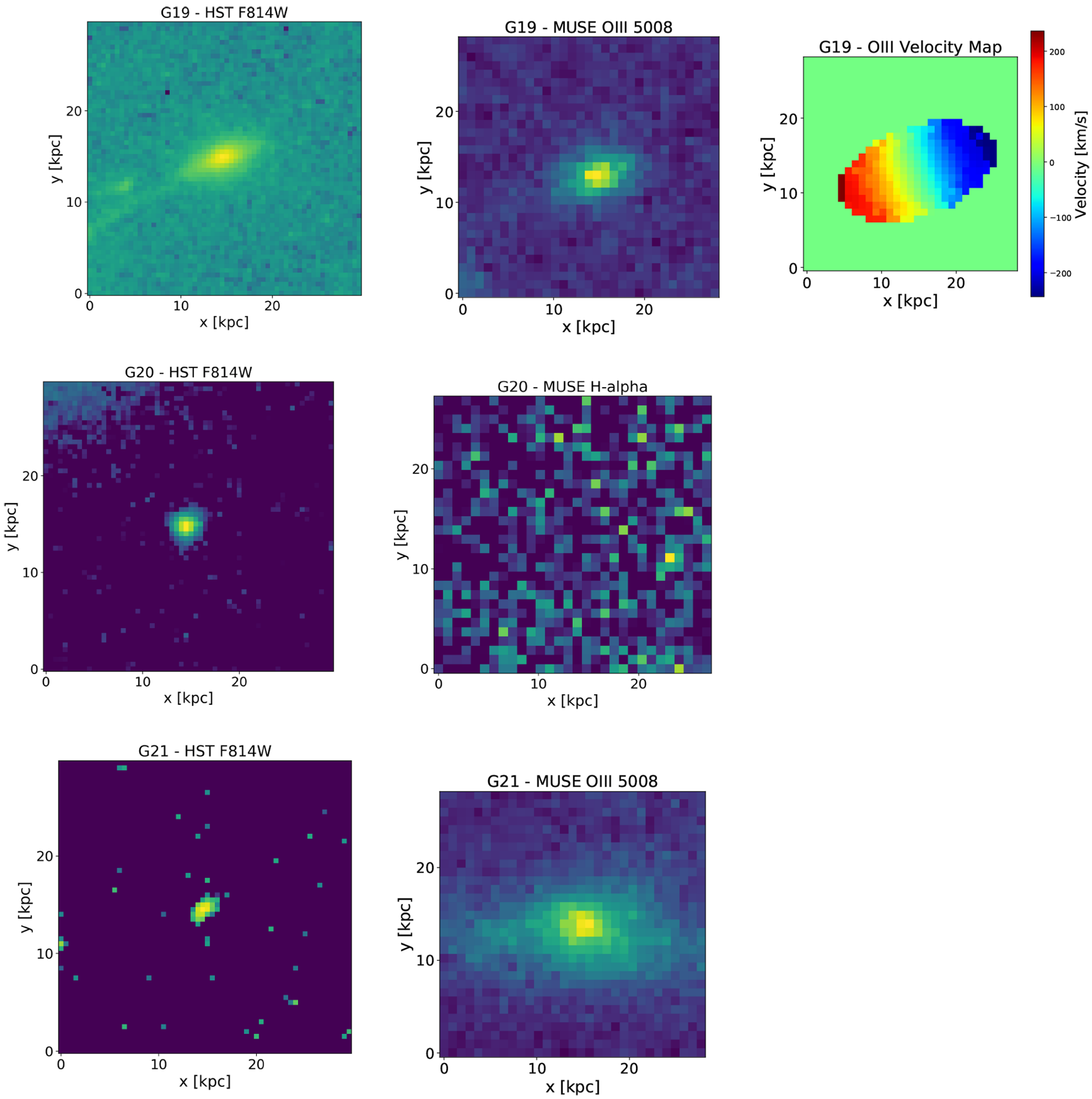

Figure B1 – *Continued*

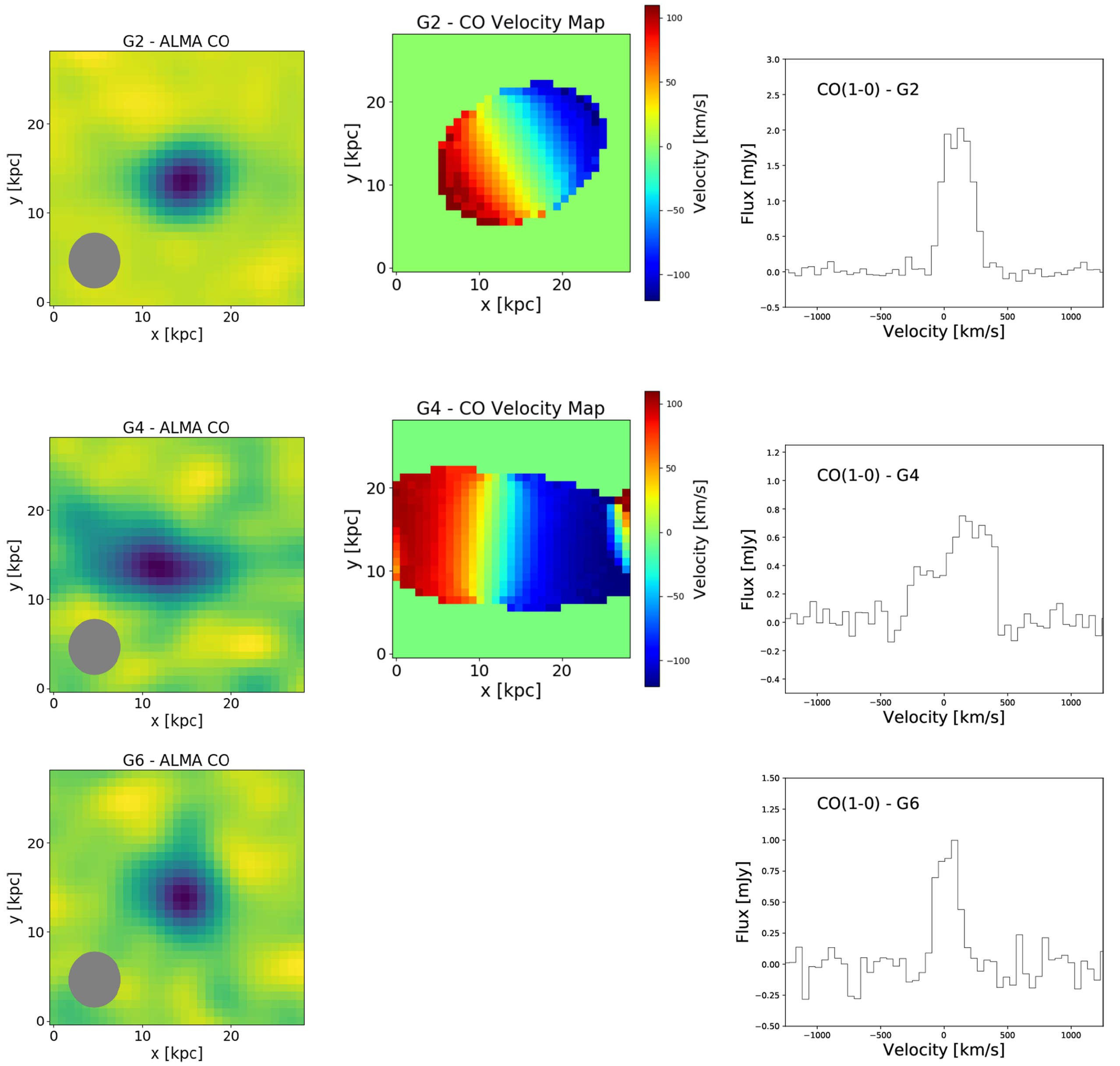

Figure B2. Molecular gas content of individual galaxies detected in ALMA at $z_{\rm abs} = 0.313$. The CO(1–0) emission line map (left), modelled velocity maps convolved with the instrumental PSF (centre) and extracted 1D CO(1–0) spectra (right) are shown. The grey ellipse on the left column indicates the ALMA beam size. The results of the morpho-kinematic analysis of G2 and G4 are qualitatively similar to the MUSE ones.

This paper has been typeset from a TEX/LATEX file prepared by the author.